

Forced periodic motions by solar radiation pressure around uniformly rotating asteroids

Xiaosheng Xin¹  · Daniel J. Scheeres² · Xiyun Hou¹

Received: 3 March 2016 / Revised: 18 April 2016 / Accepted: 10 May 2016 /
Published online: 3 June 2016
© Springer Science+Business Media Dordrecht 2016

Abstract Since asteroids generally have relatively weak gravity fields, solar radiation pressure (SRP) is a major perturbation for orbits in their vicinity, which under certain circumstances can be even larger than the third-body gravitational perturbations. In this work, by adopting a triaxial ellipsoid model for the asteroid and taking into account of SRP, the forced periodic motions caused by SRP around equilibrium points are studied in the body-fixed frame of the asteroid. For forced periodic motions around saddle equilibrium points, we find that the SRP does not alter their stability yet does change the morphology of the associated invariant manifolds. For forced periodic motions around center equilibrium points, different types of orbits are identified. Their stability changes with different parameters, i.e., the asteroid's shape and spin period, the latitude of the Sun, and the magnitude of SRP. Evolution of these forced periodic motions is described in detail and some interesting phenomena are found. Stability results found for our ideal model with the Sun at a fixed distance and latitude are shown to predict stability regions in a realistic model with the Sun on inclined and elliptic orbits. Though our work is based on the simplified triaxial ellipsoid model, similar computation method and conclusions should also be applicable to real asteroids.

Keywords Asteroid exploration · Solar radiation pressure · Periodic orbit · Stability · Saddle equilibrium (SE) · Center equilibrium (CE)

1 Introduction

Over the last two decades, there have been enduring and increasing interest in asteroid exploration among different countries and space agencies. Many missions have been successfully

✉ Xiaosheng Xin
xiaoshengxin@outlook.com

¹ School of Astronomy and Space Science, Nanjing University, 163 Xianlin Avenue, Nanjing, Jiangsu, China

² Department of Aerospace Engineering Sciences, University of Colorado at Boulder, 429 UCB, Boulder, CO, USA

carried out to different asteroids with huge scientific return which has greatly enhanced our understanding of the primordial relics preserved from the formation of the Solar System. Back in 1991, the Galileo spacecraft en route to Jupiter flew by 951 Gaspra, obtaining the first close-up view of an asteroid (Belton et al. 1992), and then later encountered 243 Ida in 1993 (Belton et al. 1994). The Near Earth Asteroid Rendezvous (NEAR) Shoemaker spacecraft rendezvoused with 433 Eros in 2000 (Yeomans et al. 2000) and became the first of its kind to soft-land on an asteroid in 2001. The Hayabusa spacecraft made in-situ observation of 25143 Itokawa in 2005 (Fujiwara et al. 2006) and managed to return asteroid samples back to the Earth in 2010. The Chang'e-2 spacecraft made a close flyby of 4179 Toutatis and conducted the first space-borne observation of that asteroid in 2012 (Huang et al. 2013). The Dawn mission (Russell et al. 2007) has successfully visited the main-belt asteroid 4 Vesta (Russell et al. 2012) and is now orbiting around 1 Ceres. The Rosetta spacecraft (Glassmeier et al. 2007) has been observing 67P/Churyumov–Gerasimenko since 2014 (Taylor et al. 2015) and deployed a lander onto the comet's surface in the November of 2015 (Bibring et al. 2015). Other future missions include the Hayabusa-2 spacecraft, which was launched in 2014 and is currently on its way to the C-type near-Earth asteroid 1999 JU3 (Tsuda et al. 2013), the OSIRIS-REx spacecraft, which is due to launch in 2016 and will visit the carbonaceous, near-Earth asteroid 101955 Bennu in 2018 (Lauretta and OSIRIS-REx Team 2012), and so on. To maximize their science return, spacecraft in these missions are usually sent to orbits very close to the asteroids or even to the surfaces of them.

Asteroids generally have weak and irregular gravity fields (Werner and Scheeres 1996; Scheeres 2012a) due to their small mass, irregular shape and porosity (Hilton 2002; Britt et al. 2002; Ostro et al. 2002). Because of a lack in accurate information of an asteroid's gravity field, asteroid missions usually require a mapping orbit phase to gain more knowledge of its gravity field and topography. The subsequent close proximity observations of the asteroid usually employ three kinds of orbits: a circum-asteroid orbit with varying altitudes at different mission phases, such as that implemented by the Dawn spacecraft around Vesta and Ceres (Russell et al. 2007), a powered hovering orbit, such as that adopted by the Hayabusa spacecraft near Itokawa (Fujiwara et al. 2006), and a sun-terminator orbit, such as that designed for the OSIRIS-REx spacecraft (Scheeres and Sutter 2013).

As a result of the weak gravity field, the perturbation caused by SRP is usually strong and should be considered when designing these exploration orbits around asteroids. Many previous works have been done utilizing SRP for orbit design, such as hovering orbits (Morrow et al. 2001; Sawai et al. 2002; Giancotti and Funase 2012) and periodic orbits (Farrés et al. 2014; Giancotti et al. 2014; García Yáñez et al. 2015b) obtained in the Hill model, the heliotropic orbits considering SRP and J_2 term of the asteroid gravity field (Colombo et al. 2012; Lantukh et al. 2015), the terminator orbits (Scheeres 1999, 2012b; Broschart et al. 2014), and the so-called alternating SRP-enabled orbiter trajectories (García Yáñez et al. 2015a).

SRP also plays an important role in the dynamics of dust or boulders ejected from the asteroid's surface due to impact or comet nucleus surface by radial gas drag forces. Hamilton and Burns (1992) analytically and numerically studied the orbital stability zones of small particles around a spherical asteroid and determine that the SRP is very efficient in removing those particles from the circumasteroidal zone. Richter and Keller (1995) presented an analytical solution for SRP acting on dust particles around a spherical body in an eccentric orbit and applied the solution to study the evolution of particle orbits around a cometary nucleus and their stability. Work by Fulle (1997) and Scheeres and Marzari (2000) both showed that ejecta particles under the effect of SRP can be captured into bound orbits around asteroids and comets that do not reimpact for a long time.

In this paper, we focus on the dynamics of forced motion about equilibrium points of an asteroid in presence of SRP, which could potentially have applications to both mission design and the study of dynamical environment around asteroids.

In the case of no SRP or third-body perturbations, equilibrium points usually exist in the body-fixed frame of a uniformly rotating asteroid. Depending on the shape and spin rate, some asteroids may possess more than four equilibrium points (Magri et al. 2007; Wang et al. 2014), but four equilibrium points are universal due to the universal non-spherical gravity of the 2nd-order and -degree gravitational field coefficients. Using a triaxial ellipsoid model for the asteroid and assuming that the asteroid is rotating about its shortest axis, Scheeres (1994) showed that the stability properties of these equilibrium points may change with the shape and spin rate of the asteroid. While the two equilibrium points on the longest axis (saddle equilibrium points, SE points) are always unstable, the two equilibrium points on the intermediate axis (center equilibrium points, CE points) can be stable for ellipsoids of certain shapes and spin rates and may become unstable when the ellipsoid becomes more elongated or its spin rate becomes faster.

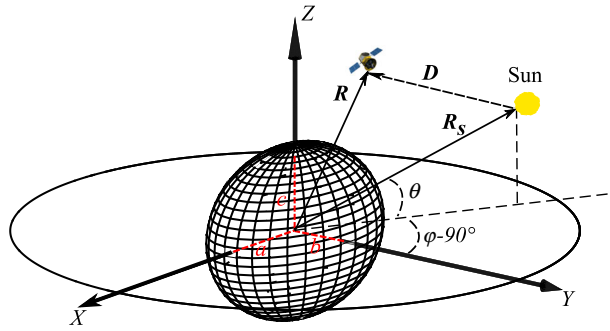
When SRP or third-body perturbations are considered, the equilibrium points usually no longer exist. Nevertheless, forced motions around the original geometrical equilibrium points appear. In some literature (Gómez et al. 2003; Hou and Liu 2010, 2011; Chappaz and Howell 2015), these forced motions are called “dynamical substitutes”. For the simplified model in this contribution, these forced motions appear as periodic orbits. They are numerically computed and their stability properties are carefully studied. The results show that the stability properties of the forced periodic motions around the SE points remain unchanged with SRP, whereas the stability properties of those around the CE points can be changed by SRP. For forced periodic motions around the CE points, by changing the latitude of the Sun in the body-fixed frame of the asteroid as well as the magnitude of SRP, different families of orbits are studied. Some interesting results are obtained:

1. As the ellipsoid becomes more elongated, fewer stable planar forced periodic orbits exist.
2. Stable planar forced periodic motions are found both for the stable and unstable CE points with the right combination of parameters, i.e., the spin period of the asteroid and the magnitude of SRP.
3. Two types of families of 3D forced periodic motions are identified, i.e., the “Type I” family and “Type II” family, and they are closely related to each other. For a given solar latitude, three forced periodic orbits may exist, two belonging to one type and the remaining one belonging to the other.
4. Stability of those ideal orbits could translate into stability for “real” systems.

One issue worth mentioning here is that the eclipse effect of the SRP is considered in our study and this consideration requires more efforts in computing the forced periodic motions and their stability parameters.

The paper is organized as follows. In Sect. 2, a simple dynamical model with the SRP is introduced by neglecting the third-body perturbation of the Sun and assuming a circular orbit of the asteroid around the Sun. In Sect. 3, some computational details are given, including the algorithm to deal with eclipse effect of SRP. Results for the families of forced periodic motions are put forward together with the analysis of their stability in Sect. 4. We discuss the results in Sect. 5 and apply those results to a more realistic model. We conclude in Sect. 6.

Fig. 1 Schematic illustration of the dynamical model



2 Dynamical model

We illustrate in detail the dynamical model that our work is based on in this section.

2.1 Ellipsoidal asteroid model

A uniformly rotating triaxial ellipsoid model is adopted for the asteroid in our study. The model is constructed in the asteroid’s body-fixed frame shown in Fig. 1. The X axis points along the asteroid’s longest axis, the Z axis along the spin axis, which is also the shortest axis, and the Y axis completes the right-handed system. The three semi-axes are a, b and c, respectively, and $a \geq b \geq c$. With a taken as the length scale, the three nondimensional semi-axes of the ellipsoid are denoted as α , which is always equal to unity, β and γ . The time scale is taken as $1/\omega$ in which $\omega = 2\pi/T$ with ω and T being the asteroid spin rate and spin period, respectively.

The nondimensional equations of motion (EOMs) involving only the gravity of the asteroid are

$$\begin{cases} \ddot{X} - 2\dot{Y} = \frac{\partial U}{\partial X} \\ \ddot{Y} + 2\dot{X} = \frac{\partial U}{\partial Y} \\ \ddot{Z} = \frac{\partial U}{\partial Z} \end{cases}, \tag{1}$$

where the effective potential U (Scheeres 1994) is defined as

$$U = \frac{1}{2}(X^2 + Y^2) - \tau V \tag{2}$$

$$V = \frac{3}{4} \int_u^\infty \phi(X, Y, Z; v) \frac{dv}{\Theta(v)} \tag{3}$$

$$\Theta(v) = \sqrt{(\alpha^2 + v)(\beta^2 + v)(\gamma^2 + v)} \tag{4}$$

$$\phi(X, Y, Z; v) = \frac{X^2}{\alpha^2 + v} + \frac{Y^2}{\beta^2 + v} + \frac{Z^2}{\gamma^2 + v} - 1 \tag{5}$$

$$\phi(X, Y, Z; u) = 0 \tag{6}$$

$$\tau = \frac{\mu}{\omega^2 a^3}. \tag{7}$$

Table 1 Values of Characteristic Spin Periods of Asteroids of Different Shapes

$\beta : \gamma$	τ_c	τ_r
0.9:0.6	2.58	3.16
0.8:0.6	4.50	6.44
0.7:0.6	6.45	9.98
0.6:0.6	8.34	13.47

$\mu = GM$ is the gravitational parameter of the asteroid with G being the gravitational constant and M being the mass of the ellipsoid. τV is the nondimensional potential of the ellipsoid. The integral in Eq. (3) is evaluated using Carlson’s elliptic integrals (Press et al. 1992) and its lower limit u is the largest positive real root of Eq. (6).

The parameter τ in Eq. (7) can also be written as

$$\tau = \alpha\beta\gamma \left(\frac{T}{T_0} \right)^2, \tag{8}$$

where

$$T_0 = \frac{2\pi}{\sqrt{\frac{4}{3}\pi G\rho}} \tag{9}$$

is the period of the orbit around the surface of an arbitrary spherical body with the same density ρ as the ellipsoid. Eq. (8) clearly shows that τ is a function of the ellipsoid’s spin period T , and thus this nondimensional parameter is adopted to represent T in the following. Some of the values of τ for different asteroid missions are listed in Table 2 in Appendix 1.

As studied by Scheeres (1994), the SE points are always unstable whereas the CE points may be stable (Type I asteroid) or unstable (Type II asteroid) depending on the shape and spin period of the asteroid. For the Type I asteroid, for motions in the equatorial plane there are two fundamental frequencies ω_{long} and ω_{short} with $\omega_{\text{long}} < \omega_{\text{short}}$ associated with the CE points. We define “resonance spin period” τ_r as the spin period of a Type I asteroid when $\omega : \omega_{\text{long}} = 2 : 1$ is satisfied. The importance of this spin period will be shown in Sect. 4.2.1. As the spin rate increases, the CE points will become unstable. The “critical spin period” τ_c is defined as the spin period when an asteroid would make transition from Type I to Type II. Some values of both the resonance spin periods and critical spin periods for ellipsoids of different shapes are listed in Table 1.

2.2 SRP model

Since the mean motion of the asteroid around the Sun is generally much smaller than the spin rate of the asteroid, we initially neglect the asteroid’s orbital motion when studying the dynamics around it within a short time interval, i.e., during this time interval the Sun’s position is assumed “frozen” in inertial space. Therefore, in the body-fixed frame of the asteroid, the Sun is on a circular orbit perpendicular to the asteroid’s spin axis, with constant latitude θ and time-varying longitude $\varphi = -\omega t + \varphi_0$ with φ_0 being the initial value as depicted in Fig. 1. Thus, the direction vector of the Sun is

$$\hat{\mathbf{R}}_s = \frac{\mathbf{R}_s}{R_s} = \begin{pmatrix} l_x \\ l_y \\ l_z \end{pmatrix} = \begin{pmatrix} \cos \theta \cos \varphi \\ \cos \theta \sin \varphi \\ \sin \theta \end{pmatrix}, \tag{10}$$

where \mathbf{R}_s is the position vector of the Sun and $R_s = \|\mathbf{R}_s\|$.

The potential function of the SRP is

$$V_{\text{SRP}} = -\frac{\rho_{\text{SRP}}}{D}, \tag{11}$$

where $D = \|\mathbf{D}\|$ with $\mathbf{D} = \mathbf{R} - \mathbf{R}_s$ and \mathbf{R} being the position vector relative to the asteroid center and the SRP parameter is

$$\rho_{\text{SRP}} = \sigma Q P_{\text{SRP}} R_{\text{SRP}}^2, \tag{12}$$

where Q is the SRP coefficient with 1 for a perfectly absorbing surface and 2 for the case of ideal specular reflection, $P_{\text{SRP}} = 4.56 \mu\text{N m}^{-2}$ is the solar pressure at $R_{\text{SRP}} = 1 \text{ AU}$ (McInnes 1999), and σ is the effective area-to-mass ratio of the space object and is assumed here as constant. For a space object with $\sigma = 0.01 \text{ m}^2 \text{ kg}^{-1}$, the SRP parameter $\rho_{\text{SRP}} \sim 1 \times 10^6 \text{ km}^3 \text{ s}^{-2}$. Since $R = \|\mathbf{R}\|$ satisfies $R \ll R_s$, the potential function of SRP can be approximated to 2nd-order as

$$V_{\text{SRP}} = V_{\text{SRP}}^{(1)} + V_{\text{SRP}}^{(2)}, \tag{13}$$

where

$$\begin{aligned} V_{\text{SRP}}^{(1)} &= -\frac{\rho_{\text{SRP}}}{R_s^3} \mathbf{R} \cdot \mathbf{R}_s \\ V_{\text{SRP}}^{(2)} &= \frac{\rho_{\text{SRP}}}{2R_s^3} \left[\mathbf{R} \cdot \mathbf{R} - 3(\mathbf{R} \cdot \hat{\mathbf{R}}_s)^2 \right]. \end{aligned} \tag{14}$$

The potential function of the third-body gravitational perturbation of the Sun is

$$V_{\text{Sun}} = \mu_s \left(\frac{1}{D} - \frac{\mathbf{R} \cdot \mathbf{R}_s}{R_s^3} \right). \tag{15}$$

It can also be approximated as

$$V_{\text{Sun}} = -\frac{\mu_s}{2R_s^3} \left[\mathbf{R} \cdot \mathbf{R} - 3(\mathbf{R} \cdot \hat{\mathbf{R}}_s)^2 \right], \tag{16}$$

where the solar gravitational parameter $\mu_s = 1.33 \times 10^{11} \text{ km}^3 \text{ s}^{-2}$.

Therefore

$$\begin{aligned} \frac{V_{\text{Sun}}}{V_{\text{SRP}}^{(1)}} &\sim \frac{\mu_s R}{\rho_{\text{SRP}} R_s} \\ \frac{V_{\text{Sun}}}{V_{\text{SRP}}^{(2)}} &\sim \frac{\mu_s}{\rho_{\text{SRP}}}. \end{aligned} \tag{17}$$

For a space object with an area-to-mass ratio $\sigma = 0.01 \text{ m}^2 \text{ kg}^{-1}$ orbiting around an asteroid with radius of tens of kilometers, the third-body gravitational perturbation of the Sun is approximately two orders of magnitude smaller than the first term of the SRP but much larger than its second term. For our dynamical model, we only keep the first term of the SRP and neglect the effect of the third-body gravitational perturbation of the Sun, although we incorporate them later in evaluating the robustness of our results.

Hence, the simplified SRP after taking into account of the eclipse effect of the Sun is

$$\mathbf{F}_{\text{SRP}} = \nu \left(\frac{\partial V_{\text{SRP}}}{\partial \mathbf{R}} \right)^T = -\frac{\nu \rho_{\text{SRP}}}{R_s^2} \hat{\mathbf{R}}_s = \nu \mathbf{F}'_{\text{SRP}}, \tag{18}$$

where ν is the eclipse factor, which is described next.

2.3 Eclipse model

Both the cylindrical and conical solar eclipse model were adopted in the work by [García Yárnoz et al. \(2015a\)](#) and they concluded that the difference between both models is negligible. However, the shadow considered in their work is projected by a spherical asteroid. In our study we assume the cylindrical solar eclipse model and propose a method to account for the shadow projected by an ellipsoidal asteroid.

At any given time, the half-line starting from the position of the space object $R = (X, Y, Z)^T$ in the direction of the Sun is

$$\begin{cases} X' = X + l_x \cdot s \\ Y' = Y + l_y \cdot s \\ Z' = Z + l_z \cdot s \end{cases}, \tag{19}$$

where $s \in [0, +\infty)$ is the half-line parameter. The function for the ellipsoid is

$$\frac{X'^2}{\alpha^2} + \frac{Y'^2}{\beta^2} + \frac{Z'^2}{\gamma^2} = 1. \tag{20}$$

Combining Eqs. (19) and (20) yields the quadratic equation of s for the intersection points of the half-line and the ellipsoid

$$As^2 + 2Bs + C = 0, \tag{21}$$

where

$$\begin{cases} A = \frac{l_x^2}{\alpha^2} + \frac{l_y^2}{\beta^2} + \frac{l_z^2}{\gamma^2} \\ B = \frac{l_x X}{\alpha^2} + \frac{l_y Y}{\beta^2} + \frac{l_z Z}{\gamma^2} \\ C = \frac{X^2}{\alpha^2} + \frac{Y^2}{\beta^2} + \frac{Z^2}{\gamma^2} - 1 \end{cases}. \tag{22}$$

The criterion for the space object to be in eclipse is that there are two real positive roots for Eq. (21). Thus, the mathematical condition for eclipse is

$$v = \begin{cases} 0 & \mathcal{D} > 0 \text{ and } \mathcal{B} < 0 \\ 1 & \text{else} \end{cases}, \tag{23}$$

where

$$\mathcal{D} = \mathcal{B}^2 - \mathcal{A}\mathcal{C}. \tag{24}$$

The eclipse factor v can be further expressed with the two-dimensional Heaviside function as

$$v = 1 - H(\mathcal{D}, -\mathcal{B}). \tag{25}$$

Details about the Heaviside function can be found in [Bracewell \(2000\)](#). Here the zero point of the Heaviside function is undefined since $\mathcal{D} = 0$ and $-\mathcal{B} = 0$ cannot be satisfied at the same time. We note that when $-\mathcal{B} = 0$ is satisfied, $\mathcal{D} < 0$.

Finally, we arrive at the EOMs taking SRP into account

$$\begin{cases} \ddot{X} - 2\dot{Y} = \frac{\partial U}{\partial X} - \nu\epsilon \cos\theta \cos\varphi \\ \ddot{Y} + 2\dot{X} = \frac{\partial U}{\partial Y} - \nu\epsilon \cos\theta \sin\varphi \\ \ddot{Z} = \frac{\partial U}{\partial Z} - \nu\epsilon \sin\theta \end{cases}, \tag{26}$$

where $\epsilon = \rho_{\text{SRP}}/(\omega^2 a R_s^2)$ is the nondimensional magnitude of the SRP. Some of the values of $\kappa = \epsilon \times 10^3$ for different asteroid missions are listed in Table 2 in Appendix 1. The strength of SRP for natural bodies near the target asteroids with radius $r_{\text{particle}} = 1$ mm and the same density as the target asteroids are also listed in Table 2. For a spherical dust particle, the area-to-mass ratio $\sigma = 3/(4\rho r_{\text{particle}})$. Note that the values vary drastically mainly due to the diverse physical properties of the target asteroids.

It is worth pointing out that Eq. (26) is symmetric with respect to the $X - Y$ plane, i.e., the asteroid’s equatorial plane. This indicates that only scenarios with solar latitude $0^\circ \leq \theta \leq 90^\circ$ need to be considered in our study. In addition, Eq. (26) is also symmetric about X axis when $\varphi_0 = 0^\circ, 180^\circ$ and symmetric about Y axis when $\varphi_0 = \pm 90^\circ$. With these symmetries, the dynamics about the pair of SE/CE points is the same and only one in each pair needs to be focused on, and the state variables can be reduced when computing corresponding forced periodic orbits.

3 Methodology

The computation algorithms to obtain the forced periodic motions together with their monodromy matrices are given in this section.

3.1 Computation algorithm

With SRP taken into account, Eq. (26) becomes time-dependent and generally equilibrium points no longer exist. However, some forced motions caused by the SRP exist. Since the Sun follows a periodic circular orbit in our simplified model, these forced motions are actually periodic orbits, with periods T_p commensurable with the asteroid’s spin period T . In our work, we only focus on the specific case with $T_p = T$.

The state of the periodic orbit

$$\mathbf{X} = (X, Y, Z, \dot{X}, \dot{Y}, \dot{Z})^T \tag{27}$$

should satisfy the periodic constraint

$$\mathbf{X}(T_p + t_0) = \mathbf{X}(t_0) = \mathbf{X}_0 \tag{28}$$

at any arbitrary time t_0 . To impose the necessary phase constraint on the solutions of the periodic orbits and take advantage of the symmetry of the dynamical system, the initial longitude of the Sun φ_0 is fixed to be 180° for the SE points and -90° for the CE points.

Predictor-corrector continuation algorithms are needed to solve Eq. (28). The Newton–Raphson correction method serves as a robust corrector in our study. For the choice of predictor, a simple version is firstly adopted. Suppose a periodic orbit that satisfies both Eqs. (26) and (28) is known and is denoted by (\mathbf{X}_0^1, q_1) , where q_1 is the continuation parameter which could be either the magnitude of the SRP ϵ (κ) or the solar latitude θ depending on

the family of forced periodic motions to be computed. For another periodic orbit (X_0^2, q_2) satisfying Eqs. (26) and (28)

$$X_0^2 = X_0^1 + \Delta X_0 \quad q_2 = q_1 + \Delta q, \tag{29}$$

the predicted approximate correction $\Delta \bar{X}_0$ can be obtained by solving

$$\left(\frac{\partial \Phi}{\partial X} \Big|_{X_0^1, q_1} - I \right) \Delta \bar{X}_0 + \frac{\partial \Phi}{\partial q} \Big|_{X_0^1, q_1} \Delta q = 0, \tag{30}$$

where Φ is the state transition matrix (STM). $\Delta \bar{X}_0$ can be used as initial guess to substitute into the correction procedure to compute the true value ΔX_0 . This predictor is straightforward and easy to implement yet may lose track of the bifurcation branch and even fail when bifurcation is encountered. When bifurcation occurs, a pseudo-arclength continuation method (Keller 1977) is adopted instead to obtain complete families of forced periodic motions.

To start the Newton–Raphson correction algorithm, an initial guess for the state of the forced periodic motion can be provided by the linear solution to the EOMs. When the SRP is small, the forced periodic motion should be close enough to the equilibrium point. Therefore, the state of the forced periodic motion can be written as

$$\bar{X} = (X_E + \xi, Y_E + \eta, Z_E + \zeta, \dot{\xi}, \dot{\eta}, \dot{\zeta})^T, \tag{31}$$

where $(X_E, Y_E, Z_E)^T$ is the position of the equilibrium point and $(\xi, \eta, \zeta)^T$ is the corresponding small deviation. The small deviation can be obtained from the variational equations

$$\begin{cases} \ddot{\xi} - 2\dot{\eta} = l\xi - v\epsilon \cos \theta \cos \varphi \\ \ddot{\eta} + 2\dot{\xi} = m\eta - v\epsilon \cos \theta \sin \varphi, \\ \ddot{\zeta} = n\zeta - v\epsilon \sin \theta \end{cases} \tag{32}$$

where

$$l = \frac{\partial^2 U}{\partial x^2} \Big|_E \quad m = \frac{\partial^2 U}{\partial y^2} \Big|_E \quad n = \frac{\partial^2 U}{\partial z^2} \Big|_E \tag{33}$$

are evaluated at the equilibrium point. One particular solution is

$$\begin{cases} \xi = (A_1 \cos \varphi + B_1 \sin \varphi) \cos \theta \\ \eta = (A_2 \cos \varphi + B_2 \sin \varphi) \cos \theta \\ \zeta = C \sin \theta \\ \dot{\xi} = (-A_1 \sin \varphi + B_1 \cos \varphi) \cos \theta \\ \dot{\eta} = (-A_2 \sin \varphi + B_2 \cos \varphi) \cos \theta \\ \dot{\zeta} = 0 \end{cases} \tag{34}$$

with the coefficients

$$\begin{cases} A_1 = \frac{m - 1}{lm + l + m - 3} v\epsilon \\ B_2 = \frac{l - 1}{lm + l + m - 3} v\epsilon \\ A_2 = B_1 = 0 \\ C = \frac{v\epsilon}{n} \end{cases} \tag{35}$$

when the condition $lm + l + m - 3 \neq 0$ is satisfied.

3.2 Stability evaluation

We analyze the stability of the forced periodic motion by evaluating the eigenvalues of the associated monodromy matrix. For a periodic orbit, the monodromy matrix is defined as the STM mapped over one period (Scheeres 2012a) and, due to the time periodic dynamical system it will not generically have unity eigenvalues. The differential equation for STM $\Phi_{6 \times 6}$ is

$$\dot{\Phi}_{6 \times 6} = A_{6 \times 6} \Phi_{6 \times 6}, \tag{36}$$

where

$$A_{6 \times 6} = \begin{pmatrix} 0_{3 \times 3} & I_{3 \times 3} \\ G_{3 \times 3} + K_{3 \times 3} & J_{3 \times 3} \end{pmatrix} \tag{37}$$

with

$$G_{3 \times 3} = \begin{pmatrix} U_{xx} & U_{xy} & U_{xz} \\ U_{yx} & U_{yy} & U_{yz} \\ U_{zx} & U_{zy} & U_{zz} \end{pmatrix} \tag{38}$$

being the matrix of second-order partial derivatives of the effective potential of the ellipsoid U with respect to the position vector \mathbf{R} ,

$$K_{3 \times 3} = \frac{\partial \mathbf{F}_{SRP}}{\partial \mathbf{R}}, \tag{39}$$

$$J_{3 \times 3} = \begin{pmatrix} 0 & 2 & 0 \\ -2 & 0 & 0 \\ 0 & 0 & 0 \end{pmatrix}, \tag{40}$$

and $I_{3 \times 3}$ being the identity matrix.

As our SRP model Eq. (18) shows, SRP is related to the direction vector of the Sun $\hat{\mathbf{R}}_s$ which is only a function of time. Therefore, when the eclipse factor ν takes values of 0 or 1, $K_{3 \times 3} = 0$. However, on the boundary of the eclipse, the eclipse factor ν defined by Eq. (25) is dependent on the position vector \mathbf{R} , which results in $K_{3 \times 3} \neq 0$. This requires an additional term $\Phi_{3 \times 6}(t^*)$ to be added at the time of eclipse boundary crossing time t^* during the integration of STM. Neglecting this additional term results in error in the computation of the monodromy matrix and the corresponding eigenvalues. Since the perturbation magnitude of the SRP is large for motions around asteroids, this error is large and should be treated with care. The expression for $\Phi_{3 \times 6}(t^*)$ can be given analytically and detailed derivation is carried out in Appendix 2.

After obtaining the monodromy matrix, stability of the forced periodic motions can be studied by analyzing the corresponding eigenvalues. For stable forced periodic motions the modulus of all eigenvalues should be equal to unity, while for unstable ones the modulus of at least one eigenvalue should be greater than one.

4 Forced periodic motions and stability

For our dynamical model, there are five free parameters, i.e., the ellipsoid shape parameters β and γ , the spin period of the ellipsoid represented by τ , the nondimensional SRP parameter ϵ (κ) that is adopted to represent the magnitude of the SRP, and the latitude of the Sun θ . Different combinations of parameters would produce distinct dynamical environments, resulting in diverse families and properties of forced periodic motions. This requires

a large parameter space to be explored. To save space, we only present some selected results.

4.1 Forced periodic motions about the SE points

For the case without SRP, motions around the SE points are unstable. There are stable and unstable invariant manifolds associated with the SE points or orbits around them (Herrera-Sucarrat et al. 2014). The incorporation of the SRP destroys the equilibrium points but doesn't change the stability property of the forced periodic motions. Similarly, we can compute the invariant manifolds associated with the forced periodic orbits. Figure 2 shows a planar periodic orbit about the SE point for solar latitude $\theta = 0^\circ$ and its corresponding unstable and stable manifold trajectories both with an integration time of 8τ .

For the dynamical model without the SRP, Herrera-Sucarrat et al. (2014) have studied the behaviour of the invariant manifolds of various SE points and related periodic orbits and their possible impact regions on the ellipsoidal asteroid. In addition, the invariant manifolds are used to design asteroid rendezvous and landing trajectory from a Lyapunov orbit around the SE point. When the SRP is taken into account, dynamics of invariant manifolds originating from periodic orbits of the forced motions should be different, and the same design method can be employed to find asteroid rendezvous and landing trajectories, which could be a subject for future study.

4.2 Forced periodic motions about the CE points

In the present work, we mainly focus on the forced periodic motions of the CE points. We first study the families of planar forced periodic motions for solar latitude $\theta = 0^\circ$. Then we extend our study to families of 3D force periodic motions with $\theta \neq 0$.

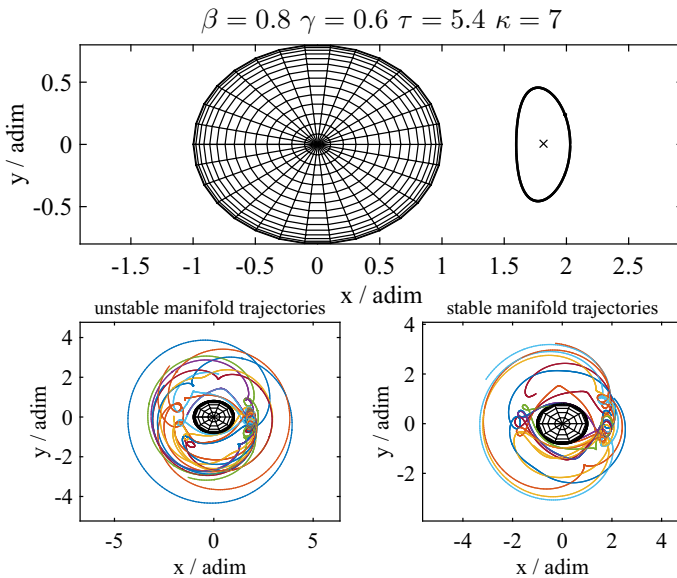


Fig. 2 A planar forced periodic orbit about the SE point (*upper panel*) and the corresponding unstable and stable manifold trajectories both with an integration time 8τ (*lower panels*). The black cross symbol denotes the SE point in the case without SRP

4.2.1 Planar forced periodic motions

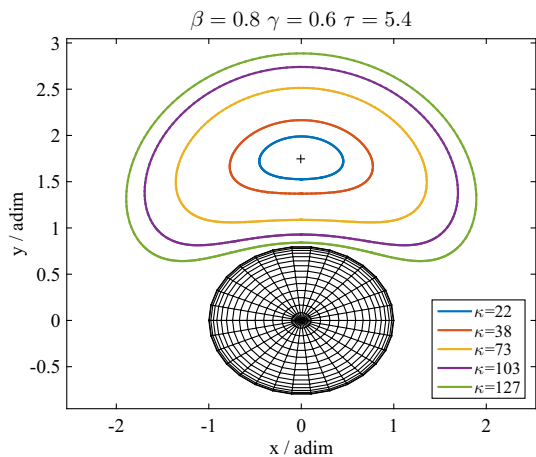
Given an asteroid with certain shape (β and γ) and spin period (τ), a family of planar forced periodic motions exist around the CE points. Each member in the family corresponds to a given magnitude of SRP κ . A sample of planar forced periodic motions of the same family are shown in Fig. 3. The forced motions are periodic orbits which all lie in the equatorial plane of the ellipsoid. As κ increases the amplitudes of the forced periodic motions become larger, and eventually the forced periodic motion will collide with the ellipsoid.

By using the simple version of the predictor-corrector continuation algorithm introduced in Sect. 3.1 and the magnitude of the SRP κ as continuation parameter, we obtain a series of families of planar forced periodic motions for ellipsoids with $\gamma = 0.6$, β taking values 0.9, 0.8, 0.7 and 0.6, and different spin periods. We evaluate the stability of each one of the forced periodic orbits and show the results as stability maps in Fig. 4. Different colors indicate planar forced periodic motions with different planar and vertical stability conditions. Red is for the planar and vertically unstable forced periodic motions, blue for the planar and vertically stable ones, yellow for the planar unstable but vertically stable ones, and green for the planar stable but vertically unstable ones. The white is for the forced periodic motions that collide with the ellipsoid. It has to be pointed out that the zigzag-shaped boundaries of the colored regions are due to the limited sampling of parameters.

Three interesting phenomena are evident in the stability maps.

1. Smooth transition of different colored regions is evident. As β becomes smaller, the red region starts to appear (top right panel in Fig. 4), then extends to the lower left of the map, with some part of its intersection with the yellow and blue region turning into green region (bottom left panel in Fig. 4), and eventually dominates the stability map together with the green region (bottom right panel in Fig. 4). This indicates that as the ellipsoid becomes more elongated, while the structure of the planar stability of the planar forced periodic motions remains qualitatively unchanged for the values we study, the vertically unstable region enlarges and the vertical stability is more affected and finally destroyed. It is interesting that though the forced periodic motions are restricted in the equatorial plane, the vertical stability can be greatly influenced by SRP.
2. The stable regions are strongly influenced by certain resonant term of SRP. The bottoms of each gap in the stable regions, which are coincident with the grey lines with circles in

Fig. 3 A family of planar forced periodic motions. The *black plus symbol* represents the CE point in the case without SRP and the same denotations apply in the following figures



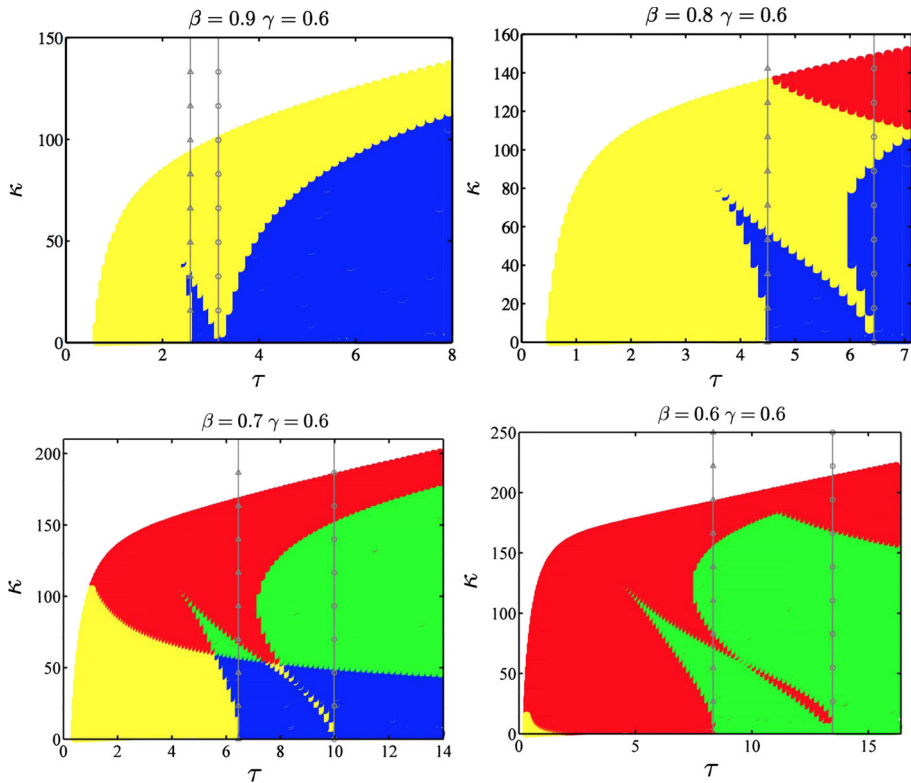


Fig. 4 Stability maps of planar forced periodic motions for ellipsoids of different shapes. *Red* is for the planar and vertically unstable forced periodic motions, *blue* for the planar and vertically stable ones, *yellow* for the planar unstable but vertically stable ones, and *green* for the planar stable but vertically unstable ones. The *white* is for the forced periodic motions that collide with the ellipsoid. The *grey lines* with *triangles* and *circles* denote the location of the critical spin period τ_c and resonance spin period τ_r on the horizontal axis of each ellipsoid, respectively

the stability maps, lie at the resonance spin periods τ_r of the ellipsoids. However, other resonant terms do not seem to play a role here.

3. In the case of no SRP, the CE points corresponding to ellipsoids with spin periods $\tau < \tau_c$ on the left of the grey lines with triangles are all unstable. However, the existence of blue regions on the left of those lines indicate that the inclusion of SRP could make certain motions around unstable CE points become stable. In fact, these stable forced periodic motions gain their stability via the generalized Hopf bifurcation (Seydel 2010).

Careful examination of the evolution of the eigenvalues of the monodromy matrices shows that bifurcations are common. Whenever the vertical stability changes, vertical bifurcation branch of the planar forced periodic motions with non-zero Z-axis position vector component appears. An example is shown in Fig. 5. The bifurcation branch starts at $\kappa = 127$ and all the vertical branch of the forced periodic motions corresponding to $\kappa < 127$ can be obtained by using pseudo-arclength continuation method. Due to the symmetry pointed out earlier, symmetric orbits with respect to the $X - Y$ plane exist. Similarly, planar bifurcations may give rise to the period-doubling forced periodic orbits, which we do not consider in this study.

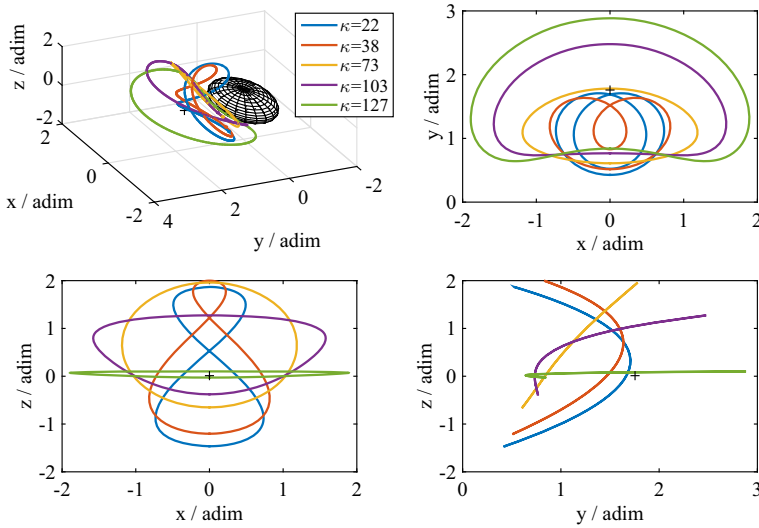


Fig. 5 Vertical bifurcation branch corresponding to the family of planar forced periodic motions in Fig. 3

4.2.2 3D forced periodic motions

In the case where the latitude of the Sun $\theta \neq 0$, the forced periodic motions are generally not restrained to lie in the equatorial plane of the asteroid. Due to the symmetry with respect to the ellipsoid’s equatorial plane, we only consider cases with solar latitude in the range $0^\circ < \theta \leq 90^\circ$. Given an asteroid with certain shape (β and γ) and spin period (τ) in presence of certain magnitude of SRP κ , different families of 3D forced periodic motions may exist. Each member in the same family corresponds to a given solar latitude θ .

Intuitively, these 3D forced periodic motions can be obtained by continuation from the corresponding planar forced periodic motions taking the latitude of the Sun θ as the continuation parameter. Families of 3D forced periodic motions computed in this way are called “Type I” families. For $\beta : \gamma = 0.8 : 0.6$ $\tau = 4.0$ $\kappa = 70$, this whole family is obtained and represented by the blue characteristic curve (maximum value of z -component z_{\max} versus solar latitude θ) in Fig. 6. It is obvious from the figure that this Type I family of 3D forced periodic motions exists for the whole range of solar latitudes and remain stable for solar latitudes up to $\sim 4^\circ$. There is also a stable interval for solar latitudes between $\sim 22^\circ$ and $\sim 46^\circ$. When the Sun is right above the ellipsoid ($\theta = 90^\circ$), the forced periodic motion shrinks to a single point. It is worth mentioning that as the solar latitude increases, the eclipse conditions of the dynamical substitutes also change from partial shadow to no shadow. This transition causes the little dip shown in the blue characteristic curve.

However, for larger SRP strength, Type I families of forced periodic motions may no longer exist for solar latitude higher than a certain value. This is clearly shown in Fig. 7 by the blue characteristic curve of the Type I family with $\kappa = 97$. This of course does not mean that the forced periodic orbits do not exist for high solar latitude.

To find forced periodic motions for higher solar latitude in the case $\kappa = 97$, continuation procedure starting from the solar latitude $\theta = 90^\circ$ downward is adopted instead. As mentioned before, when $\theta = 90^\circ$, the 3D forced periodic motion degenerates to be a single point near the corresponding CE point. The approximate initial state can be given by Eq. (34). For large

Fig. 6 Characteristic curves of 3D forced periodic motions. The blue line is for the Type I family and the red line for the Type II family. The solid and dashed lines represent forced periodic motions that are stable and unstable, respectively, and the same denotations apply in the following figures

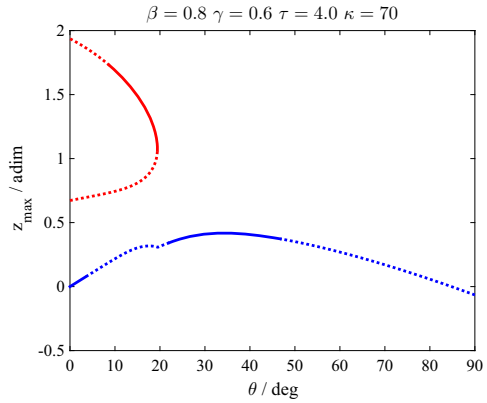
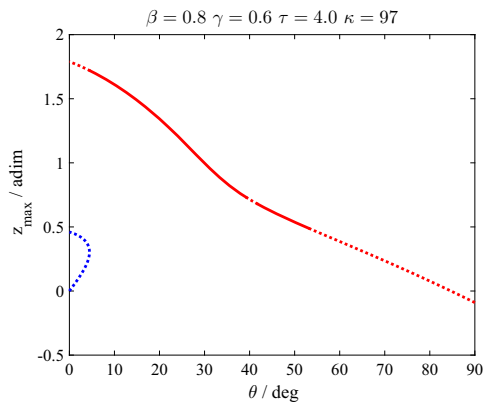


Fig. 7 Characteristic curves of 3D forced periodic motions. The blue line is for the Type I family and the red line for the Type II family



magnitudes of SRP such as $\kappa = 97$, a new family of 3D forced periodic motions can be obtained in this way and is called “Type II” family. The whole family is represented by the red characteristic curve in Fig. 7. In fact, we can continue from the members with small solar latitudes belonging to the Type II family for $\kappa = 97$ and compute the forced periodic motions of the same family for other smaller magnitudes of SRP, e.g., $\kappa = 70$, which is shown by the red characteristic curve in Fig. 6.

It should be noted that when the solar latitude $\theta = 90^\circ$ the equilibrium point generally exists. It is located where the gravity force of the asteroid, the centrifugal force, and the SRP balance. It coincides with the CE point when the SRP is zero. The equilibrium point belongs to the Type I family when SRP is small and the Type II family when SRP is large. The critical value of SRP for this transition to occur depends on the parameters of the asteroid and an example is given later in Fig. 12.

Comparing Figs. 6 and 7, it is obvious that three forced periodic orbits may exist for the same solar latitude, two of which belong to the same family (either Type I or Type II) due to the bifurcation of the fold points type (Seydel 2010). In addition, shown from those three figures, forced periodic motions of Type II family are generally unstable when the solar latitude θ is close to 0° or 90° , whereas forced periodic motions of Type I family can be stable for solar latitudes from 0° up to several degrees or more depending on the choice of parameters.

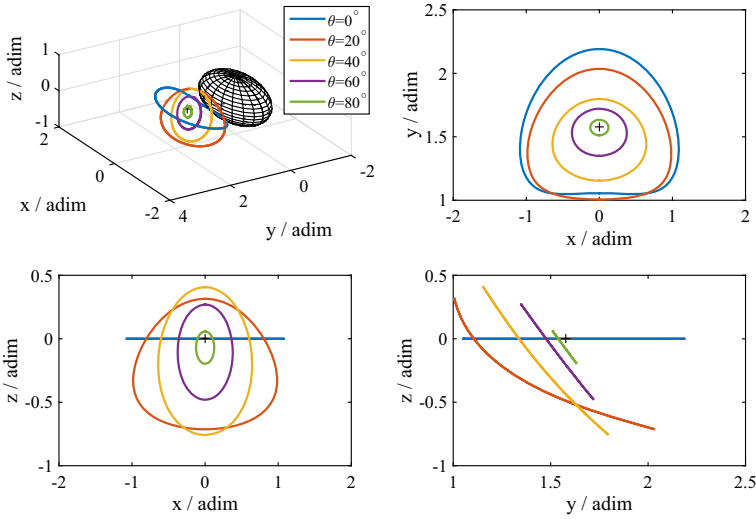


Fig. 8 A Type I family of 3D forced periodic motions for $\beta : \gamma = 0.8 : 0.6$ $\tau = 4.0$ $\kappa = 70$

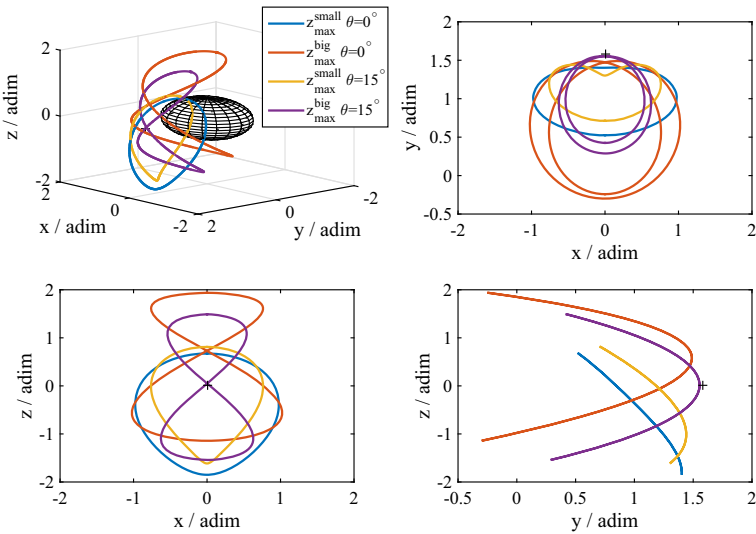


Fig. 9 A Type II family of 3D forced periodic motions for $\beta : \gamma = 0.8 : 0.6$ $\tau = 4.0$ $\kappa = 70$. z_{\max}^{small} denotes the forced periodic motions corresponding to the lower branch of the red line with smaller values of z_{\max} and z_{\max}^{big} denotes the forced periodic motions corresponding to the upper branch of the red line with larger values of z_{\max} in Fig. 6

We show some members of the two families of forced periodic motions for the cases $\beta : \gamma = 0.8 : 0.6$ $\tau = 4.0$ with $\kappa = 70$ and $\kappa = 97$ respectively in Figs. 8, 9, 10 and 11. It is worth noting that the periodic orbits of the forced motions of Type II family normally have figure-eight shape which could extend to the polar region of the ellipsoid. In addition, the Type II family generally has larger z_{\max} than that of the Type I family, especially for lower solar latitude. These features distinguish the Type II family from the Type I family.

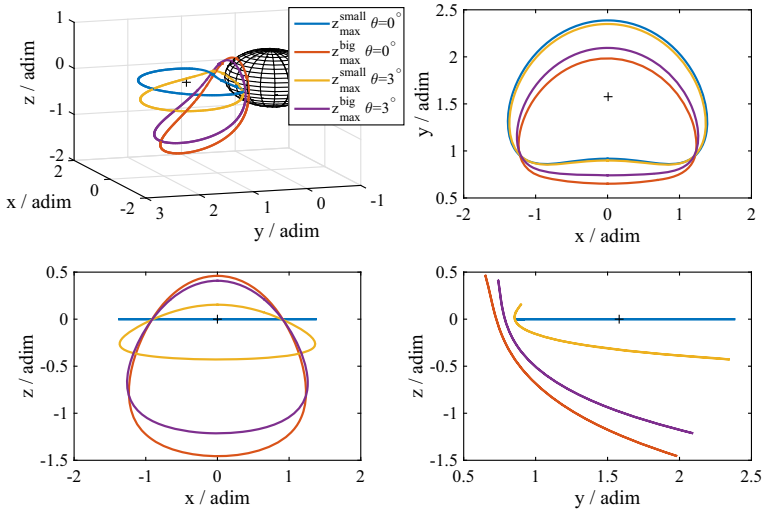


Fig. 10 A Type I family of 3D forced periodic motions for $\beta : \gamma = 0.8 : 0.6$ $\tau = 4.0$ $\kappa = 97$. z_{\max}^{small} denotes the forced periodic motions corresponding to the lower branch of the blue line with smaller values of z_{\max} and z_{\max}^{big} denotes the forced periodic motions corresponding to the upper branch of the blue line with larger values of z_{\max} in Fig. 7

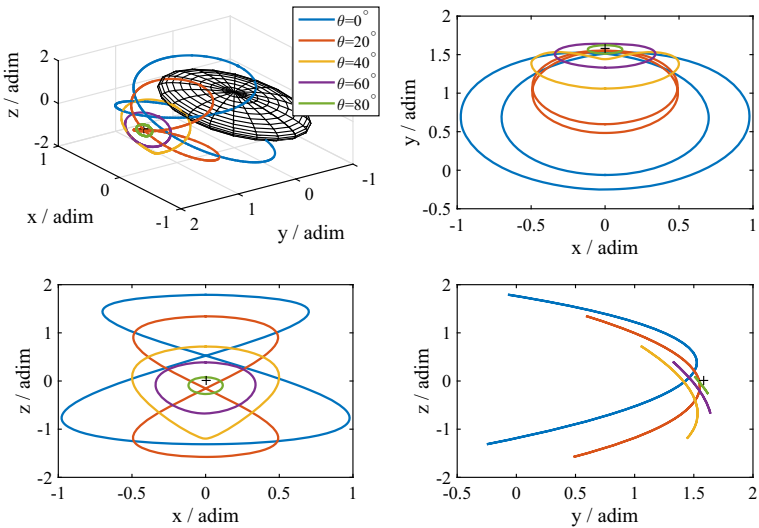


Fig. 11 A Type II family of 3D forced periodic motions for $\beta : \gamma = 0.8 : 0.6$ $\tau = 4.0$ $\kappa = 97$

Detailed computation also shows that both the Type I and Type II families of the forced periodic motions are common for ellipsoids of different shapes and spin periods. Moreover, we find that these two families are related to each other as we gradually change the magnitude of the SRP, which is shown in Fig. 12. Clearly, the characteristic curves of the two families break and reconnect with one another as the SRP increases from $\kappa = 77.1$ to $\kappa = 77.6$. This kind of phenomena is quite common among studies of other dynamical systems, such as the

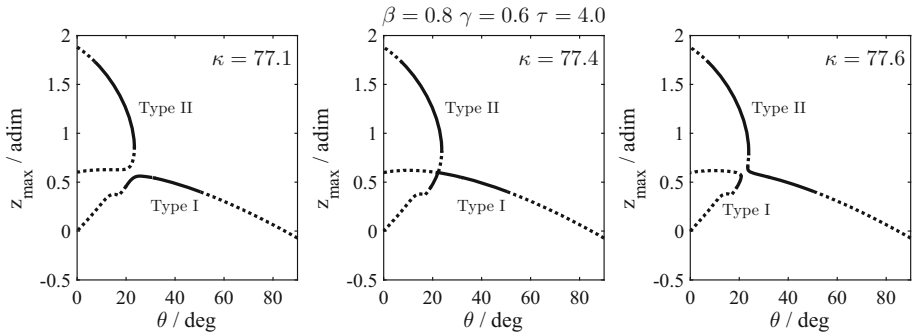


Fig. 12 Evolution of characteristic curves for Type I and Type II family of forced periodic motions as the magnitude of the SRP changes

study of planar Lyapunov families around collinear libration points in the circular restricted three-body problem (CRTBP) by [Hou and Liu \(2009\)](#).

5 Discussion

Based on the simplified model we have obtained families of forced periodic motions around asteroids and studied their stability properties. As pointed out by [Scheeres et al. \(2000\)](#), the study of stability of periodic orbit families can be a useful approach to the stability characterization of orbits about an asteroid. The stability of the forced periodic motions can be directly related to the expected stability properties of the neighboring motions, and can even provide knowledge of stability for motions in the real dynamical model.

Compared with the real dynamical model around an asteroid, the simplified model in our work neglects the following perturbations: (1) non-ellipsoidal gravity terms caused by the real shape of the asteroid; (2) the third-body perturbation from the Sun; (3) higher order terms of the SRP; (4) the orbital motion of the asteroid around the Sun.

In our work, we use a triaxial ellipsoid to simulate the shape and the gravity of an asteroid, but the real case is much more complicated than a triaxial ellipsoid. Generally, for motions very close to the asteroid, specific treatment should be made for each individual asteroid. It is hard to reach a general conclusion if details of each asteroid are considered. So in this work we neglect these details and simply use the triaxial ellipsoid model to get some general conclusions. Besides, with more efforts, the method in this work (i.e., computing the forced periodic motions and the stability parameters) can be generalized to a real asteroid. In the same sense, since our study only focuses on the natural dynamics of forced periodic motions around asteroids, discussions of those practical aspects that involve spacecraft operations and control, such as changes in effective area-to-mass ratio, are left out in our work.

As for the third-body perturbation of the Sun and the higher order terms of SRP, as we already pointed out at the beginning of this work, they are much smaller than the term considered for the SRP in this work and will not qualitatively change our conclusions. What is more impactful are the changing solar latitude and varying distance from the Sun due to the real asteroid's orbital motion. These factors do affect the dynamics of the forced periodic motions. However, our conclusions obtained from the simplified model can provide guidance in understanding the effect of these factors. This is verified by the following numerical simulations.

5.1 Real dynamical model

We construct a more realistic model that incorporates the higher order terms of SRP, the third-body perturbation of the Sun, and the orbital motion of the asteroid.

The nondimensional EOMs in the asteroid-centered inertial frame is given by

$$\ddot{\mathbf{r}} = -\tau \left(\frac{\partial V}{\partial \mathbf{r}} \right)^T - \left(\psi_1 \hat{\mathbf{r}}_s + \psi_2 \hat{\mathbf{d}} \right) + \nu \psi_3 \hat{\mathbf{d}}, \tag{41}$$

where V and τ are already given in Eqs. (3) and (7), respectively, and

$$\hat{\mathbf{r}}_s = \frac{\mathbf{r}_s}{r_s} \quad \hat{\mathbf{d}} = \frac{\mathbf{d}}{d} \tag{42}$$

with $\mathbf{d} = \mathbf{r} - \mathbf{r}_s$, \mathbf{r} and \mathbf{r}_s being the position vectors of the space object and the Sun relative to the center of the asteroid in the inertial frame, respectively, $r_s = \|\mathbf{r}_s\|$ and $d = \|\mathbf{d}\|$. The nondimensional parameters are defined as

$$\psi_1 = \frac{\mu_s}{\omega^2 a r_s^2} \quad \psi_2 = \frac{\mu_s}{\omega^2 a d^2} \quad \psi_3 = \frac{\rho_s}{\omega^2 a d^2}. \tag{43}$$

Note that the three terms on the right side of Eq. (41) represent the gravitational force of the asteroid, the perturbation of the Sun, and SRP, respectively. Since V is evaluated in the body-fixed frame of the asteroid, the computation of the gravitational force of the asteroid in the inertial frame also involves coordinate transformation from the body-fixed frame to the inertial frame.

From the perspective of the asteroid, the Sun is in circular motion about it with the latitude θ and longitude φ computed from

$$\sin \theta = \sin i \sin \tilde{u} \tag{44}$$

and

$$\varphi = \varphi_1 + \varphi_0 \quad \sin \varphi_1 = \frac{\tan \theta}{\tan i} \quad \cos \varphi_1 = \frac{\cos \tilde{u}}{\cos \theta}, \tag{45}$$

where i is the obliquity between asteroid’s orbital plane and its equatorial plane and \tilde{u} is the argument of latitude of the Sun.

5.2 Effect of orbital obliquity

If we consider the asteroid’s circular orbital motion and its obliquity i , the Sun’s latitude is no longer fixed in the body-fixed frame of the asteroid. When the Sun is in the asteroid’s equatorial plane, $\theta = 0^\circ$; when the Sun passes the upper or lower culmination point, the Sun’s latitude θ reaches its maximum value ($\theta_{max} = i$ for prograde motion and $\theta_{max} = 180^\circ - i$ for retrograde motion) or its minimum value ($\theta_{min} = -i$ for prograde motion and $\theta_{min} = i - 180^\circ$ for retrograde motion). However, due to the fact that the spin period of the asteroid is usually much smaller than its orbital period, during a short time interval (e.g., several spin periods), the Sun’s latitude can still be taken as constant and the stability properties of the forced periodic motions we have obtained in this study should therefore be applicable. This indicates that as long as there exist a series of forced periodic motions for solar latitudes in the range $0^\circ \leq |\theta| \leq \theta^*$ in our simplified model, these forced periodic motions may remain stable in the real dynamical model with the obliquity $i \leq \theta^*$ for prograde orbital motion and $180^\circ - i \leq \theta^*$ for retrograde orbital motion.

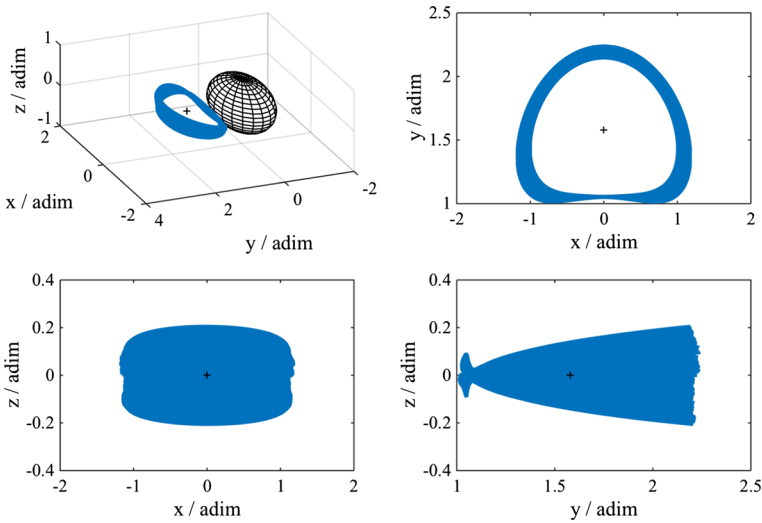


Fig. 13 Stable region within which all the integrated trajectories of the forced periodic motions lie. These periodic orbits belong to the Type I family of the 3D forced periodic motions for the case $\beta : \gamma = 0.8 : 0.6$ $\tau = 4.0$ $\kappa = 70$ $\theta_s = 3^\circ$. The trajectories are integrated for 1 year, and the orbit obliquity $i = 4^\circ$

To verify our conclusions, we take the forced periodic orbits in the Type I family which are stable for solar latitudes $0^\circ \leq |\theta| \leq \theta^*$ and integrate them in the inertial frame for 1 year by using the Eq. (41) with the obliquity fixed to $i = \theta^*$ and \vec{u} changing with time from 0° to 360° . If the integrated trajectories of the periodic orbits for solar latitudes $\theta \leq \theta_s$ do not collide with the ellipsoid during the time and stay within certain finite region, we are confident that these forced periodic motions are indeed stable over the timespan of 1 year. Nominally θ_s is not equal to θ^* due to the discrepancy between our simplified model and the real model. Here we only need to focus on the cases corresponding to the prograde motion, i.e., $i < 90^\circ$.

For the case $\beta : \gamma = 0.8 : 0.6$ $\tau = 4.0$ $\kappa = 70$, forced periodic motions in the Type I family are stable for $\theta^* = 4^\circ$ (see Fig. 6). The stable region of all the stable forced periodic motions for $\theta_s = 3^\circ$ with $i = 4^\circ$ is shown in the rotating frame in Fig. 13. This result clearly supports our conclusions. However, when the obliquity $i > 4^\circ$, the forced periodic motions lose their stability and the integrated trajectories may collide with the ellipsoid in the end, which is shown in Fig. 14 as an example for the forced periodic orbits of $\theta = 3^\circ$ with $i = 5^\circ$. The trajectory impacts the ellipsoid within 0.3 year. This is easy to understand. Since for this case $\theta_{max} = 5^\circ > \theta^*$, the perturbation of SRP destabilizes the forced periodic motions around the asteroid during the period when $i > 4^\circ$, which is corroborated by the fact that no stable forced periodic motions exist for solar latitudes between $\sim 4^\circ$ and $\sim 22^\circ$ shown by the blue characteristic curve in Fig. 6.

In addition, it needs to be pointed out that stable region could also exist about the equilibrium points of an asteroid for obliquity i taking values as large as tens of degrees. For the case $\beta : \gamma = 0.8 : 0.6$ $\tau = 6.2$ $\kappa = 50$, as shown in Fig. 15, forced periodic motions of the Type I family are stable for $\theta^* = 15^\circ$. It is therefore reasonable to expect that in the real model these periodic orbits should be stable for fairly large orbit obliquity, which is exactly what is shown in Fig. 16 for the stable region of the forced periodic orbits for $\theta_s = 10^\circ$ with $i = 15^\circ$.

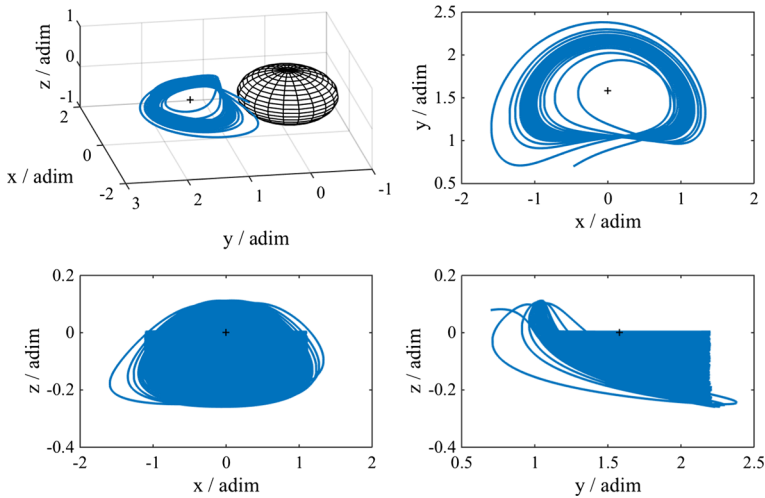
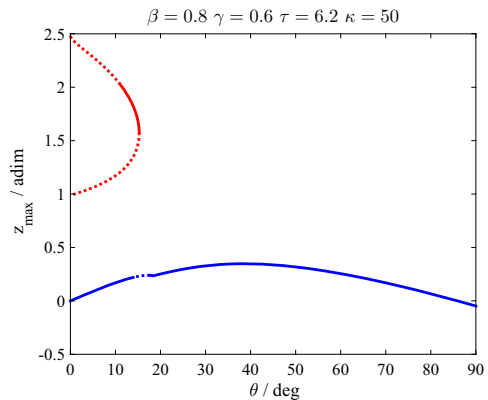


Fig. 14 The integrated trajectory of the periodic orbit of $\theta = 3^\circ$ that collides with the ellipsoid for the case $\beta : \gamma = 0.8 : 0.6$ $\tau = 4.0$ $\kappa = 70$. The orbit obliquity $i = 5^\circ$, and the impact time is less than 0.3 year

Fig. 15 Characteristic curves of 3D forced periodic motions. The blue line is for the Type I family and the red line for the Type II family



5.3 Effect of orbital eccentricity

Another issue when considering the asteroid’s orbital motion is the orbital eccentricity e . It’s easy to understand that the SRP reaches its maximum when the asteroid is at its perigee and its minimum at the apogee, and that the variation is dependent on the value of eccentricity. In order for the forced periodic motions to remain stable around an asteroid with elliptical orbital motion, the eccentricity should not exceed a certain value. For the case of stable planar forced periodic motions, suppose the upper and lower bound of the SRP for a certain family is κ_{max} and κ_{min} (the blue region in Fig. 4), the maximum eccentricity e_{max} is constrained by the relation

$$e_{max} = \frac{\sqrt{\kappa_{max}} - \sqrt{\kappa_{min}}}{\sqrt{\kappa_{max}} + \sqrt{\kappa_{min}}}. \tag{46}$$

For an asteroid with orbital eccentricity $e \leq e_{max}$, there should exist stable forced periodic motions in the simplified model that remain stable in the real model as long as they are ensured

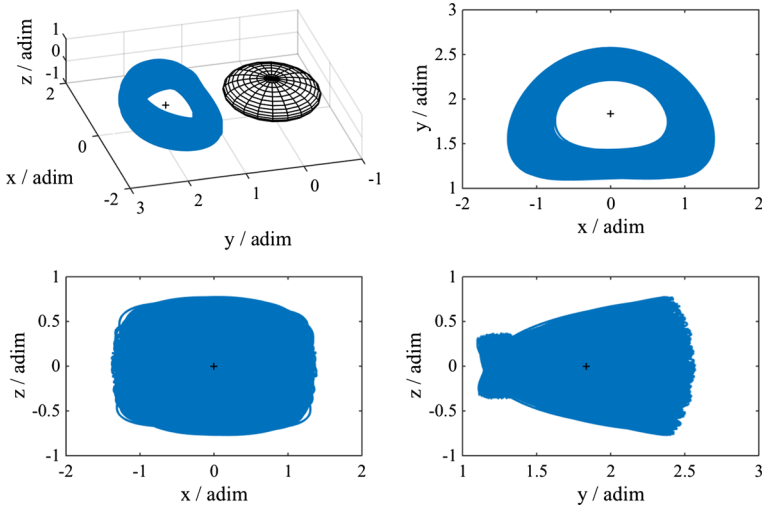


Fig. 16 Stable region within which all the integrated trajectories of the forced periodic motions lie. These periodic orbits belong to the Type I family of the 3D forced periodic motions for the case $\beta : \gamma = 0.8 : 0.6$ $\tau = 6.2$ $\kappa = 50$ $\theta_s = 10^\circ$. The trajectories are integrated for 1 year, and the orbit obliquity $i = 15^\circ$

to experience SRP of magnitude κ in the range $\kappa_{min} \leq \kappa \leq \kappa_{max}$ during the revolution of the asteroid.

We illustrate this with the numerical simulation of the planar forced periodic motions for the case $\beta : \gamma = 0.8 : 0.6$ $\tau = 5.4$ as an example. The upper and lower bound of the SRP for the forced periodic motions to be stable is $\kappa_{max} \sim 38$ and $\kappa_{min} \sim 0$. The maximum eccentricity is, therefore, $e_{max} \sim 0.5$.

We choose eccentricity $e = 0.4$ such that the magnitude of SRP is $\kappa_p \sim 38$ at perigee and $\kappa_a \sim 7$ at apogee. The corresponding stable planar forced periodic motions of κ in the range $7 \leq \kappa \leq 38$ are integrated in the inertial frame for 1 year by using Eq. (41) with obliquity fixed $i = 0^\circ$ and \tilde{u} changing with time for a total of 360° . The initial position of the asteroid in its orbit is chosen dependent on each planar forced periodic motion of κ that is integrated such that the magnitude of SRP at that point is exactly κ . The results show that for planar forced periodic motions of $\sim 7 \leq \kappa \leq \sim 14$, all the integrated trajectories lie within the blue region shown in the rotating frame in Fig. 17, which proves that these forced periodic motions can remain stable in the real model considering the elliptical orbital motion of the asteroid. Moreover, the stable region seems well bounded by the corresponding planar forced periodic motions of $\kappa = 38$. In addition, it needs to be pointed out that the integrated trajectories of the planar forced periodic motions of $\sim 0 \leq \kappa \sim 7$ could also remain within the blue region in the real model given the same range of SRP and orbital eccentricity.

Other planar forced periodic motions of $\sim 14 < \kappa < \sim 38$ collide with the asteroid in less than 1 year as an example for $\kappa = 15$ shows in Fig. 18. It is evident that once the integrated trajectory wanders out of the region enclosed by the planar forced periodic motions of $\kappa = 38$, it quickly inflates in amplitude and impacts with the asteroid in the end. We speculate that this phenomenon is closely related to the stability widths of the planar forced periodic motions in the real model and the detailed analysis requires further study.

Generally, the existence of stable regions in the real model is dependent on the parameters of the asteroid and the space object, which hence requires a case by case study. [Scheeres et al.](#)

Fig. 17 Stable region of the integrated trajectories of the stable planar forced periodic motions of $\sim 7 \leq \kappa \leq \sim 14$ for the case $\beta : \gamma = 0.8 : 0.6$ $\tau = 5.4$. The orbit eccentricity $e = 0.4$ and the trajectories are integrated for 1 year. The red line represents the planar forced periodic motion of $\kappa = 38$ obtained in the simplified model

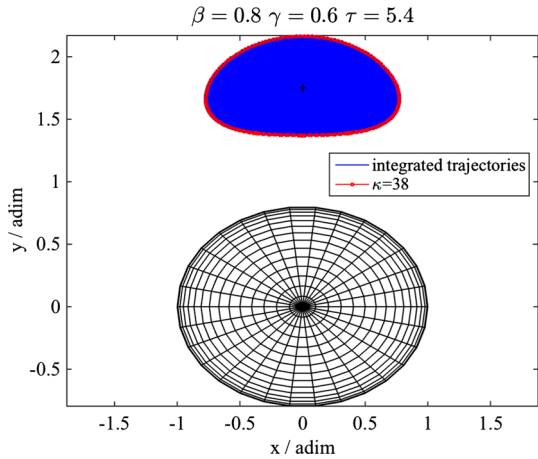
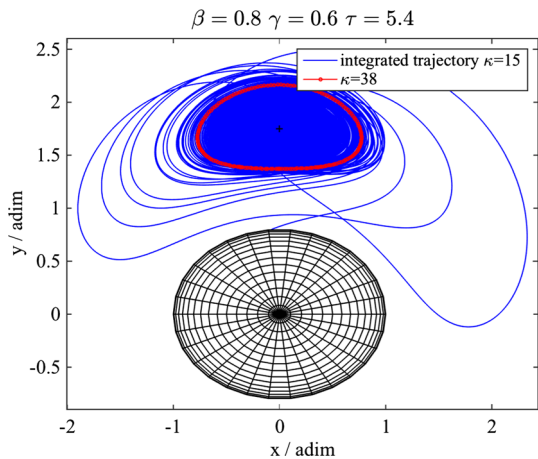


Fig. 18 The integrated trajectory of the stable planar forced periodic motions of $\kappa = 15$ for the case $\beta : \gamma = 0.8 : 0.6$ $\tau = 5.4$. The orbit eccentricity $e = 0.4$. The trajectory collides with the asteroid in 0.8 year. The red line represents the planar forced periodic motion of $\kappa = 38$ obtained in the simplified model



(2002) reviewed the dynamics of ejecta around an asteroid with a classification of surface ejecta in terms of their fate. With different perturbative forces acting together, a class of long-term stable orbits for those ejecta can exist about the asteroid. The stable regions for the forced periodic motions obtained in our study could be a likely place for ejecta to stay for an extended period of time. Moreover, for space exploration application, these forced periodic motions may serve as spacecraft observation trajectories around an asteroid.

6 Conclusions

In the presence of SRP, the dynamical equations of a small body in the body-fixed frame of a uniformly rotating asteroid becomes non-autonomous and the equilibrium points no longer exist. Nevertheless, special orbits are forced to exist by the SRP. They are called forced periodic motions in this work. With reasonable simplifications of the dynamical model, i.e., triaxial ellipsoid model for the asteroid, neglecting the asteroid orbital motion in the inertial frame, lowest order approximation of SRP, and no third-body perturbation, we compute

these forced periodic motions around the equilibrium points in this simplified model. They appear as periodic orbits with the same period as the SRP. Their stability parameters are also computed via the monodromy matrix. Special treatment is given to the monodromy matrix when dealing with the eclipse of SRP, which is usually unnecessary for dynamics around major celestial bodies but critical to our study.

We find that for the SE points, the SRP does not alter the stability of the forced periodic motions yet does change the morphology and dynamics of the associated invariant manifolds. For the CE points, both planar and 3D forced periodic motions are obtained. Important conclusions include:

1. Stability conditions of the planar forced periodic motions for four representative ellipsoids are obtained, which are well illustrated by the stability map in Fig. 4. As the ellipsoid becomes more elongated, smooth transition of regions with different stability properties are observed and the stable region shrinks. The vertical stability of the planar forced periodic motions is more affected and finally destroyed by the elongation while the structure of the planar stability remains qualitatively unchanged for the values we study. In addition, the stable region is influenced by the resonance between the fundamental frequency of the CE point and that of the SRP.
2. Stable planar forced periodic motions are found both for the stable and unstable CE points with the right combination of parameters, i.e., the spin period of the asteroid and the magnitude of SRP.
3. Two types of families of 3D forced periodic motions are identified, i.e., the Type I and Type II. For a given solar latitude, three forced periodic orbits may exist, two belonging to one type and the remaining one belonging to the other. These two types of families are related to each other, which are shown clearly by their respective characteristic curve.
4. Given certain combination of parameters, forced periodic motions of the Type I family can be stable for solar latitudes up to tens of degrees in our simplified model. Numerical simulations based on the real model taking into account of the asteroid's orbital motion are carried out and the conclusion is verified. The results show that stable regions can exist in the real model for orbital obliquity as large as tens of degrees and orbital eccentricity ~ 0.4 for certain asteroid. These results provide insights into the dynamics of asteroid's ejecta as well as trajectory design for asteroid missions.

Though our work is based on the simplified triaxial ellipsoid model, the conclusions can be referenced for motions around real asteroids. Also, the method in this work can be plainly generalized to real asteroids.

Acknowledgments This work was finished during the first author's visit to the Colorado Center for Astrodynamics Research (CCAR). X.S.X thanks Nicola Baresi, David Surovik and Inkwan Park for their valuable discussions and help during the visit. X.S.X and X.Y.H thank the support from National Natural Science Foundation of China (11322330) and National Basic Research Program of China (2013CB834100). All authors thank the anonymous reviewers for their invaluable comments.

Appendix 1: Table of τ and κ for selected asteroid missions

See Table 2.

Table 2 Nondimensional values of target asteroids’ spin periods and SRP strengths on spacecraft and natural bodies for different asteroid missions

Mission	NEAR ^a	Dawn ^b	Hayabusa ^c	OSIRIS-REx ^d
Target asteroid	Eros	Vesta	Itokawa	Bennu
R_S (AU)	1.46	2.36	1.32	1.13
a (km)	20	280	0.25	0.25
$\beta : \gamma$	0.28:0.26	0.97:0.78	0.54:0.41	0.97:0.90
T (h)	5.27	5.34	12.13	4.30
ρ (g cm ⁻³)	2.67	3.46	1.90	1.26
τ	0.6	6.8	5.7	1.9
S/C σ (m ² kg ⁻¹)	0.018	0.045	0.030	0.014
κ ($\epsilon \times 10^3$)	1.7×10^{-2}	1.2×10^{-3}	15.3	1.2
Natural body σ (m ² kg ⁻¹)	0.281	0.217	0.395	0.595
κ ($\epsilon \times 10^3$)	2.7×10^{-1}	5.9×10^{-3}	200	52

^a Yeomans et al. (2000), Zuber et al. (2000), Cheng (1997)

^b Russell et al. (2012), Thomas et al. (2011)

^c Fujiwara et al. (2006), Kawaguchi et al. (2006)

^d Lauretta et al. (2015), Broschart et al. (2013)

Appendix 2: Derivation of $\Phi_{3 \times 6}(t^*)$

We first break STM $\Phi_{6 \times 6}$ into a partitioned matrix

$$\Phi_{6 \times 6} = \begin{pmatrix} \Phi_{3 \times 6}^1 \\ \Phi_{3 \times 6}^2 \end{pmatrix}. \tag{47}$$

Integrating Eq. (36) for one period we get

$$\begin{cases} \Phi_{3 \times 6}^1(t_0, T_p + t_0) = \int_{t_0}^{T_p+t_0} \Phi_{3 \times 6}^2 dt \\ \Phi_{3 \times 6}^2(t_0, T_p + t_0) = \int_{t_0}^{T_p+t_0} (G_{3 \times 3} \cdot \Phi_{3 \times 6}^1 + J_{3 \times 3} \cdot \Phi_{3 \times 6}^2) dt + \Phi_{3 \times 6}(t^*). \end{cases} \tag{48}$$

The integration can be carried out numerically except for

$$\Phi_{3 \times 6}(t^*) = \int_{t_0}^{T_p+t_0} K_{3 \times 3} \cdot \Phi_{3 \times 6}^1 dt \tag{49}$$

which can be given in analytical form.

Recall that only the eclipse factor ν is a function of the position vector \mathbf{R} , hence

$$K_{3 \times 3} = \frac{\partial \mathbf{F}_{SRP}}{\partial \mathbf{R}} = \mathbf{F}'_{SRP} \cdot \left[-\frac{\partial H(\mathcal{D}, -\mathcal{B})}{\partial \mathbf{R}} \right]. \tag{50}$$

According to the properties of Heaviside function $H(x, y)$ and Delta Dirac function $\delta(x)$, which are explained in detail by Bracewell (2000) in Ch. 4 & 5,

$$\frac{d}{dx} H(x, y) = \delta(x)H(y), \tag{51}$$

and

$$\int_a^b \delta [g(x)] f(x) dx = \sum_i \frac{f(x_i)}{|g'(x_i)|} \quad (52)$$

where $g(x_i) = 0$, $g'(x_i) \neq 0$ and $x_i \in (a, b)$.

Therefore, Eq. (49) becomes

$$\begin{aligned} \Phi_{3 \times 6}(t^*) &= \int_{t_0}^{T_p+t_0} \mathbf{F}'_{\text{SRP}} \cdot \left[-\delta(\mathcal{D})H(-\mathcal{B}) \frac{\partial \mathcal{D}}{\partial \mathbf{R}} - \delta(-\mathcal{B})H(\mathcal{D}) \frac{\partial(-\mathcal{B})}{\partial \mathbf{R}} \right] \Phi_{3 \times 6}^1 dt \\ &= \sum_{i=1}^2 \mathbf{F}'_{\text{SRP}}(t_i^*) \cdot \left[-\frac{\frac{\partial \mathcal{D}}{\partial \mathbf{R}}|_{t_i^*}}{|\dot{\mathcal{D}}(t_i^*)|} \right] \cdot \Phi_{3 \times 6}^1(t_i^*, t_0). \end{aligned} \quad (53)$$

This indicates that $\Phi_{3 \times 6}(t^*)$ needs to be calculated at each of the eclipse boundary crossing time t_i^* and added to STM during the integration process. Nominally, when eclipse occurs, two eclipse boundary crossings are expected and the summation is evaluated twice.

References

- Belton, M., Veverka, J., Thomas, P., Helfenstein, P., Simonelli, D., Chapman, C., et al.: Galileo encounter with 951 Gaspra: first pictures of an asteroid. *Science* **257**(5077), 1647–1652 (1992)
- Belton, M., Chapman, C., Veverka, J., Klaasen, K., Harch, A., Greeley, R., et al.: First images of asteroid 243 Ida. *Science* **265**(5178), 1543–1547 (1994)
- Bibring, J.P., Taylor, M., Alexander, C., Auster, U., Biele, J., Finzi, A.E., et al.: Philae's first days on the comet. *Science* **349**(6247), 493–493 (2015)
- Bracewell, R.N.: *The Fourier Transform and Its Applications*, 3rd edn. McGraw-Hill, New York (2000)
- Britt, D., Yeomans, D., Housen, K., Consolmagno, G.: Asteroid density, porosity, and structure. In: Bottke Jr., W.F., Cellino, A., Paolicchi, P., Binzel, R.P. (eds.) *Asteroids III*, pp. 485–500. University of Arizona Press, Tucson (2002)
- Broschart, S.B., Lantoine, G., Grebow, D.J.: Characteristics of quasi-terminator orbits near primitive bodies. In: 23rd AAS/AIAA Spaceflight Mechanics Meeting. Kauai, Hawaii (2013)
- Broschart, S.B., Lantoine, G., Grebow, D.J.: Quasi-terminator orbits near primitive bodies. *Celest. Mech. Dyn. Astron.* **120**(2), 195–215 (2014)
- Chappaz, L., Howell, K.C.: Exploration of bounded motion near binary systems comprised of small irregular bodies. *Celest. Mech. Dyn. Astron.* **123**(2), 123–149 (2015)
- Cheng, A.F.: Near Earth Asteroid Rendezvous: mission overview. *Space Sci. Rev.* **82**(1), 3–29 (1997)
- Colombo, C., Lücking, C., McInnes, C.R.: Orbital dynamics of high area-to-mass ratio spacecraft with J_2 and solar radiation pressure for novel Earth observation and communication services. *Acta Astronaut.* **81**(1), 137–150 (2012)
- Farrés, A., Jorba, À., Mondelo, J.M., Villac, B.: Periodic motion for an imperfect solar sail near an asteroid. In: Macdonald, M. (ed.) *Advances in Solar Sailing*, pp. 885–898. Springer, New York (2014)
- Fujiwara, A., Kawaguchi, J., Yeomans, D., Abe, M., Mukai, T., Okada, T., et al.: The rubble-pile asteroid Itokawa as observed by Hayabusa. *Science* **312**(5778), 1330–1334 (2006)
- Fulle, M.: Injection of large grains into orbits around comet nuclei. *Astron. Astrophys.* **325**, 1237–1248 (1997)
- García Yáñez, D., Sanchez Cuartielles, J.P., McInnes, C.R.: Alternating orbiter strategy for asteroid exploration. *J. Guid. Control Dyn.* **38**(2), 280–291 (2015a)
- García Yáñez, D., Scheeres, D.J., McInnes, C.R.: On the a and g families of orbits in the Hill problem with solar radiation pressure and their application to asteroid orbiters. *Celest. Mech. Dyn. Astron.* **121**(4), 365–384 (2015b)
- Giancotti, M., Funase, R.: Solar sail equilibrium positions and transfer trajectories close to a Trojan asteroid. In: *The 63rd International Astronautical Congress* (2012)
- Giancotti, M., Campagnola, S., Tsuda, Y., Kawaguchi, J.: Families of periodic orbits in Hill's problem with solar radiation pressure: application to Hayabusa 2. *Celest. Mech. Dyn. Astron.* **120**(3), 269–286 (2014)
- Glassmeier, K.H., Boehnhardt, H., Koschny, D., Kührt, E., Richter, I.: The Rosetta mission: flying towards the origin of the solar system. *Space Sci. Rev.* **128**(1–4), 1–21 (2007)

- Gómez, G., Masdemont, J., Mondelo, J.: Dynamical substitutes of the libration points for simplified solar system models. In: Gómez, G., Lo, M.W., Masdemont, J.J. (eds.) *Libration Point Orbits and Applications*, pp. 373–397. World Scientific, Singapore (2003)
- Hamilton, D.P., Burns, J.A.: Orbital stability zones about asteroids: II. The destabilizing effects of eccentric orbits and of solar radiation. *Icarus* **96**(1), 43–64 (1992)
- Herrera-Sucarrat, E., Palmer, P., Roberts, R.: Asteroid observation and landing trajectories using invariant manifolds. *J. Guid. Control Dyn.* **37**(3), 907–920 (2014)
- Hilton, J.L.: Asteroid masses and densities. In: Bottke Jr., W.F., Cellino, A., Paolicchi, P., Binzel, R.P. (eds.) *Asteroids III*, pp. 103–112. University of Arizona Press, Tucson (2002)
- Hou, X., Liu, L.: On Lyapunov families around collinear libration points. *Astron. J.* **137**(6), 4577 (2009)
- Hou, X.Y., Liu, L.: On quasi-periodic motions around the triangular libration points of the real Earth–Moon system. *Celest. Mech. Dyn. Astron.* **108**, 301–313 (2010). doi:[10.1007/s10569-010-9305-3](https://doi.org/10.1007/s10569-010-9305-3)
- Hou, X.Y., Liu, L.: On quasi-periodic motions around the collinear libration points in the real Earth–Moon system. *Celest. Mech. Dyn. Astron.* **110**, 71–98 (2011)
- Huang, J., Ji, J., Ye, P., Wang, X., Yan, J., Meng, L., et al.: The ginger-shaped asteroid 4179 Toutatis: new observations from a successful flyby of Chang’e-2. *Sci. Rep.* **3**, 3411 (2013)
- Kawaguchi, J., Kuninaka, H., Fujiwara, A., Uesugi, T.: MUSES-C, its launch and early orbit operations. *Acta Astronaut.* **59**(8), 669–678 (2006)
- Keller, H.B.: Numerical solution of bifurcation and nonlinear eigenvalue problems. In: Rabinowitz, P.H. (ed.) *Applications of Bifurcation theory*, pp.359–384. Academic Press, New York (1977)
- Lantukh, D., Russell, R.P., Broschart, S.: Heliotropic orbits at oblate asteroids: balancing solar radiation pressure and J_2 perturbations. *Celest. Mech. Dyn. Astron.* **121**(2), 171–190 (2015)
- Lauretta, D., Bartels, A., Barucci, M., Bierhaus, E., Binzel, R., Bottke, W., et al.: The OSIRIS-REx target asteroid (101955) Bennu: constraints on its physical, geological, and dynamical nature from astronomical observations. *Meteorit. Planet. Sci.* **50**(4), 834–849 (2015)
- Lauretta, D.S., OSIRIS-REx Team: An overview of the OSIRIS-REx asteroid sample return mission. In: *Lunar and Planetary Science Conference*, vol. 43, p. 2491 (2012)
- Magri, C., Ostro, S.J., Scheeres, D.J., Nolan, M.C., Giorgini, J.D., Benner, L.A., et al.: Radar observations and a physical model of asteroid 1580 Betulia. *Icarus* **186**(1), 152–177 (2007)
- McInnes, C.R.: *Solar Sailing: Technology, Dynamics and Mission Applications*. Springer, London (1999)
- Morrow, E., Scheeres, D.J., Lubin, D.: Solar sail orbit operations at asteroids. *J. Spacecr. Rockets* **38**(2), 279–286 (2001)
- Ostro, S.J., Hudson, R.S., Benner, L.A., Giorgini, J.D., Magri, C., Margot, J.L., Nolan, M.C.: Asteroid radar astronomy. In: Bottke Jr., W.F., Cellino, A., Paolicchi, P., Binzel, R.P. (eds.) *Asteroids III*, pp. 151–168. University of Arizona Press, Tucson (2002)
- Press, W., Teukolsky, S., Vetterling, W., Flannery, B.: *Numerical Recipes in Fortran 77: The Art of Scientific Computing*. Cambridge University Press, New York (1992)
- Richter, K., Keller, H.: On the stability of dust particle orbits around cometary nuclei. *Icarus* **114**(2), 355–371 (1995)
- Russell, C., Capaccioni, F., Coradini, A., De Sanctis, M., Feldman, W., Jaumann, R., et al.: Dawn mission to Vesta and Ceres. *Earth Moon Planets* **101**(1–2), 65–91 (2007)
- Russell, C., Raymond, C., Coradini, A., McSween, H., Zuber, M., Nathues, A., et al.: Dawn at Vesta: testing the protoplanetary paradigm. *Science* **336**(6082), 684–686 (2012)
- Sawai, S., Scheeres, D., Broschart, S.: Control of hovering spacecraft using altimetry. *J. Guid. Control Dyn.* **25**(4), 786–795 (2002)
- Scheeres, D.: Satellite dynamics about small bodies: averaged solar radiation pressure effects. *J. Astronaut. Sci.* **47**, 25–46 (1999)
- Scheeres, D.: *Orbital Motion in Strongly Perturbed Environments: Applications to Asteroid, Comet and Planetary Satellite Orbiters*. Springer, New York (2012a)
- Scheeres, D., Marzari, F.: Temporary orbital capture of ejecta from comets and asteroids: application to the deep impact experiment. *Astron. Astrophys.* **356**, 747–756 (2000)
- Scheeres, D., Williams, B., Miller, J.: Evaluation of the dynamic environment of an asteroid: Applications to 433 Eros. *J. Guid. Control Dyn.* **23**(3), 466–475 (2000)
- Scheeres, D., Durda, D., Geissler, P.: The fate of asteroid ejecta. In: Bottke Jr., W.F., Cellino, A., Paolicchi, P., Binzel, R.P. (eds.) *Asteroids III*, pp. 527–544. University of Arizona Press, Tucson (2002)
- Scheeres, D.J.: Dynamics about uniformly rotating triaxial ellipsoids: applications to asteroids. *Icarus* **110**(2), 225–238 (1994)
- Scheeres, D.J.: Orbit mechanics about asteroids and comets. *J. Guid. Control Dyn.* **35**(3), 987–997 (2012b)
- Scheeres, D.J., Sutter, B.: Design, dynamics and stability of the OSIRIS-REx sun-terminator orbits. In: 23rd AAS/AIAA Spaceflight Mechanics Meeting, Kauai, Hawaii (2013)

- Seydel, R.: *Practical Bifurcation and Stability Analysis*, 3rd edn. Springer, New York (2010)
- Taylor, M., Alexander, C., Altobelli, N., Fulle, M., Fulchignoni, M., Grün, E., et al.: Rosetta begins its comet tale. *Science* **347**(6220), 387–387 (2015)
- Thomas, V.C., Makowski, J.M., Brown, G.M., McCarthy, J.F., Bruno, D., Cardoso, J.C., et al.: The Dawn spacecraft. *Space Sci. Rev.* **163**(1), 175–249 (2011)
- Tsuda, Y., Yoshikawa, M., Abe, M., Minamino, H., Nakazawa, S.: System design of the Hayabusa 2–Asteroid sample return mission to 1999 JU3. *Acta Astronaut.* **91**, 356–362 (2013)
- Wang, X., Jiang, Y., Gong, S.: Analysis of the potential field and equilibrium points of irregular-shaped minor celestial bodies. *Astrophys. Space Sci.* **353**(1), 105–121 (2014)
- Werner, R.A., Scheeres, D.J.: Exterior gravitation of a polyhedron derived and compared with harmonic and mascon gravitation representations of asteroid 4769 Castalia. *Celest. Mech. Dyn. Astron.* **65**(3), 313–344 (1996)
- Yeomans, D., Antreasian, P., Barriot, J.P., Chesley, S., Dunham, D., Farquhar, R., et al.: Radio science results during the NEAR-Shoemaker spacecraft rendezvous with Eros. *Science* **289**(5487), 2085–2088 (2000)
- Zuber, M.T., Smith, D.E., Cheng, A.F., Garvin, J.B., Aharonson, O., Cole, T.D., et al.: The shape of 433 Eros from the NEAR-Shoemaker Laser Rangefinder. *Science* **289**(5487), 2097–2101 (2000)